



HAL
open science

Balanced charge transport optimizes industry-relevant ternary polymer solar cells

Robin Szymanski, Reece Henry, Samuel H Stuard, Uyxing Vongsaysy, Stéphanie Courtel, Luc Vellutini, Mélanie Bertrand, Harald Ade, Sylvain Chambon, Guillaume Wantz

► To cite this version:

Robin Szymanski, Reece Henry, Samuel H Stuard, Uyxing Vongsaysy, Stéphanie Courtel, et al.. Balanced charge transport optimizes industry-relevant ternary polymer solar cells. *Solar RRL*, 2020, 4 (11), pp.2000538. 10.1002/solr.202000538. hal-03420105

HAL Id: hal-03420105

<https://hal.science/hal-03420105>

Submitted on 9 Nov 2021

HAL is a multi-disciplinary open access archive for the deposit and dissemination of scientific research documents, whether they are published or not. The documents may come from teaching and research institutions in France or abroad, or from public or private research centers.

L'archive ouverte pluridisciplinaire **HAL**, est destinée au dépôt et à la diffusion de documents scientifiques de niveau recherche, publiés ou non, émanant des établissements d'enseignement et de recherche français ou étrangers, des laboratoires publics ou privés.

Balanced charge transport optimizes industry-relevant ternary polymer solar cells

Robin Szymanski, Reece Henry, Samuel Stuard, Uyxing Vongsaysy, Stéphanie Courtel, Luc Vellutini, Mélanie Bertrand, Harald Ade, Sylvain Chambon, Guillaume Wantz**

R. Szymanski, Dr. S. Chambon, Prof. G. Wantz

Univ. Bordeaux, CNRS, Bordeaux INP, IMS, UMR 5218, Talence, France

E-Mail: Guillaume.Wantz@enscbp.fr

R. Szymanski, Dr. U. Vongsaysy, Dr. S. Courtel, M. Bertrand

ARMOR SOLAR POWER FILMS SAS, Nantes (France)

R. Henry, S. Stuard, Prof. H. Ade

Department of Physics, North Carolina State University, Raleigh, North Carolina 27695, USA

Dr. L. Vellutini

Univ. Bordeaux, CNRS, Bordeaux INP, ISM, UMR 5255, F-33405 Talence, (France)

Dr. S. Chambon

LIMMS/CNRS-IIS (UMI2820), Institute of Industrial Science, University of Tokyo, 4-6-1

Komaba, Meguro-ku, Tokyo, 153-8505, Japan

Keywords: Polymer solar cells, low-cost semiconducting polymer, non-chlorinated solvent processing, ternary blend, industrial figure of merit

Abstract text

Bulk heterojunction polymer solar cells based on a novel combination of materials are fabricated using industry-compliant conditions for large area manufacturing. The relatively low-cost polymer PTQ10 is paired with the non-fullerene acceptor 4TIC-4F. Devices are processed using a non-halogenated solvent to comply with industrial usage in absence of any thermal treatment to minimize the energy footprint of the fabrication. No solvent additive is used. Adding the well-known and low-cost fullerene derivative PC₆₁BM acceptor to this binary blend to form a ternary blend, the power conversion efficiency (PCE) was improved from 8.4% to 9.9% due to increased fill factor (FF) and open circuit voltage (V_{OC}), while simultaneously improving the stability. The introduction of PC₆₁BM is able to balance the hole-electron mobility in the ternary blends, which is favourable for high FF. This charge transport behavior is correlated with the bulk heterojunction (BHJ) morphology deduced from Grazing-Incidence Wide-Angle X-ray Scattering (GIWAXS), Atomic Force Microscopy (AFM) and surface energy analysis. In addition, the industrial figure of merit (i-FOM) of this ternary blend was found to increase drastically upon addition of PC₆₁BM due to an increased performance-stability-cost balance.

Main text

1. Introduction

Solution-processed organic solar cells (OSCs) have demonstrated a drastic increase in power conversion efficiency (PCE) over the recent years thanks to a wide variety of novel organic semiconductors with novel conjugated polymers and the rise of non-fullerene acceptors (NFAs).^{[1][2][3]} NFAs have a broader light absorption than the fullerene acceptors, which leads to significant increase in short-circuit current (J_{SC}). The up-to-date record PCE in organic photovoltaics (OPV) is held by *Li et al.*^[4] with 18.2% efficiency using a new polymeric donor (D18) and the NFA named Y6^[5] also known as BTP-4F^[6] or BTPTT-4F^[7] introduced by Yuan et al^[5] (for full names, see Supporting Information). Most of the high performing conjugated

polymers in laboratory-scale research devices contain an electron-rich (push) benzodithiophene (BDT) unit or a related analogue. Combined with a relatively electron-poor (pull) building block such as benzodithiophenedione (BDD), thienothiophene (TT) or benzotriazole (BTA), high-performance push-pull copolymers were successfully designed over the last decade.^{[1][8]} Among the most efficient, the following ones can be highlighted: PBDB-T, also known as PCE-12,^[9] PBDB-T-2F, also known as PM6 or PBDB-TF,^[10] PTB7-Th,^[11] FTAZ^[12] and its derivative J71.^[13] These polymers have a high potential for the OPV industry in terms of performances. However, all these polymers are complex in terms of chemical structure, meaning that their chemical synthesis remains difficult with multiple synthesis steps with relatively low synthesis yields.^[14] As a consequence, such polymers are costly, which is not consistent with the ultimate goal of OPV to produce a low cost printed solar photovoltaic technology. In 2018, Sun *et al.*^[15] designed a promising novel and simple structure for an electron donating conjugated copolymer: Poly[(thiophene)-alt-(6,7-difluoro-2-(2-hexyldecyloxy)quinoxaline)] (PTQ10, **Figure 1**), reporting a maximum PCE of 12.7% with the NFA called IDIC. Later, Wu *et al.*^[16] demonstrated a PCE of 16.5% with the active layer PTQ10:Y6, which is among the highest reported PCE for a single junction OSC. In order to quantify this aspect, Po *et al.* introduced the synthetic complexity index (SC index) in 2015.^[17] The **Table S2** shows the calculated SC index for PTQ10 and the abovementioned polymers,^[18] confirming that PTQ10 is one of the most affordable high efficiency polymer for OPV.

In addition to this cost consideration, the commercial fabrication process of OSC needs to meet several requirements to be compatible with industrial large-scale processing. In particular, the PCE has to be insensitive – to some extent – to the thickness of the active layer. These features were demonstrated for PTQ10 with different NFAs such as IDIC, MO-IDIC-2F, *m*-ITIC-2F, *m*-ITIC-4F or IDTPC.^{[19][20][21]} However in these studies, several processing conditions such as the use of chloroform as host solvent, thermal annealing at high temperature (140 °C) or solvent

vapor annealing, appear to be non-compatible for industrial manufacture of OPV. Indeed, only a fast and low-temperature drying is acceptable in a production line when an active layer is deposited by slot-die coating on a stretched flexible substrate. Minimizing the heating during OPV fabrication processes is also important to reduce the energy footprint of this novel class of solar PV modules. Meanwhile, the ternary blend strategy has proven effective performances enhancement, while maintaining the straightforward fabrication process of OSC. In particular, adding a second acceptor in the active layer demonstrated promising PCE enhancements of several OPV devices in the literature.^[22] In most ternary blends, the second acceptor improves the J_{SC} due to a complementary absorption with the host binary blend.^{[23][24][25]} PC₆₁BM is also used in ternary blend and has proven to be an effective strategy to increase the PCE of binary blends.^{[26][27][28]}

In this work, we combined PTQ10 with the NFA 4TIC-4F (also known as F6IC, **Figure 1**) introduced by Dai *et al.*^[29] 4TIC-4F has a high electron mobility, a broad light absorption in film, and its energy levels are compatible with those of PTQ10.^{[29][30]} PTQ10 and 4TIC-4F are soluble in 1,2,4-trimethylbenzene (TMB), a high boiling point non-halogenated solvent.^[31] Using TMB to spin coat the active layer, we fabricated OSCs with an inverted structure with PCE up to 8.4 %. Subsequently, we investigated the ternary blend strategy to improve this PCE. Here, we added PC₆₁BM^[32] as a second acceptor to form ternary OSC, which has a weak absorption in the ultraviolet-visible (UV-vis) range. We selected PC₆₁BM over the typically higher performing PC₇₁BM due to its lower cost. This strategy enabled us to improve the PCE to 9.9 % due to an improved fill factor (FF) and open circuit voltage (V_{OC}). To understand these improvements, we studied the charge transport properties via the space-charge limited current (SCLC) method. It revealed that PC₆₁BM enabled a better balance between the hole mobility (μ_h) and the electron mobility (μ_e), which is beneficial for the FF. Morphological characterizations were performed using as Grazing-Incidence Wide-Angle X-ray Scattering

(GIWAXS), Atomic Force Microscopy (AFM) and contact angle. These techniques demonstrated that PC₆₁BM mixes with 4TIC-4F and the mixed PTQ10:4TIC-4F amorphous phases. This optimal mixed phases in ternary blend improves the hole transport. In addition to that, the industrial potential of this ternary blend shows promising results.

Results and discussion

1. Materials properties

Figure 1 shows the chemical structures of PTQ10, 4TIC-4F, and PC₆₁BM, their normalized UV–vis absorption spectra in thin film and in TMB solution (10^{-6} M) and their energy levels according to previous works.^{[15][30][33]} The procedures used to prepare the solutions and films are described in Supporting Information. A significant redshift of ca. 130 nm appears between the absorption spectrum of 4TIC-4F in solution state and in thin film state. This shift means that this NFA has a significant self-organization when deposited by spin coating.^[34] In other words, a close intermolecular π - π stacking appears upon drying. In thin film, 4TIC-4F absorbs in the visible and near-infrared region in the range of 650-900 nm, which is complementary with the 300-650 nm range of the wide bandgap polymer donor PTQ10. The molar extinction coefficient ϵ of 4TIC-4F was calculated via the Beer-Lambert law (**Equation S1**) from the absorbance - concentration plots in solution at their absorption maxima wavelength^[35] (**Figure S1**). We found a high ϵ of $2.71 \cdot 10^5 \text{ M}^{-1} \cdot \text{cm}^{-1}$ for 4TIC-4F. This suggests that 4TIC-4F has a high light harvesting ability, which is generally desirable to achieve high J_{SC} . These photophysical and electrochemical data are summarized in the

Table S3.

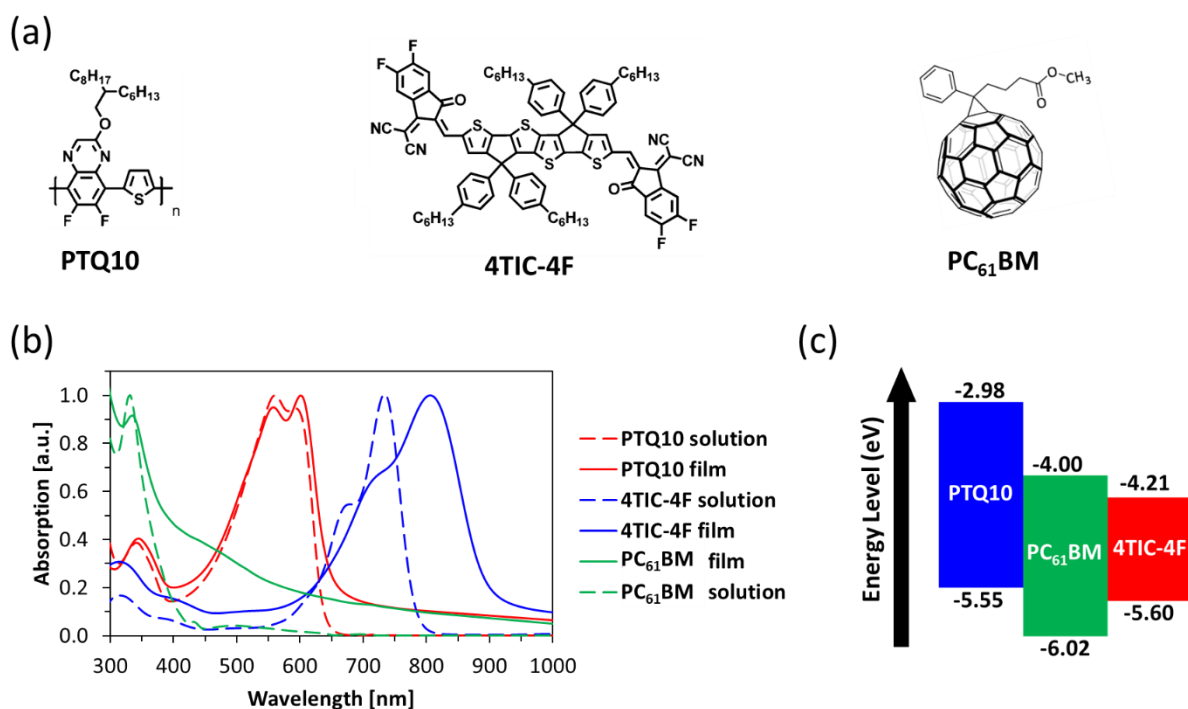


Figure 1. (a) Chemical structures of the used materials. (b) Normalized absorption in film and TMB solution of PTQ10, 4TIC-4F and PC₆₁BM. (c) Energy diagram of PTQ10, 4TIC-4F and PC₆₁BM.

2. Photovoltaic performances

To investigate the photovoltaic properties of this novel active layer composition, we fabricated OSCs using the following inverted device architecture: Indium Tin Oxide (ITO)/ZnO/active layer/MoO₃/Ag. The detailed fabrication process of OSCs and their characterizations are described in Supporting Information. The active layer was deposited by spin coating method. It should be noted that the active layer was processed in the respect of several industrial constraints: no thermal annealing nor solvent vapor annealing was applied and the ink was free from halogenated solvent and solvent additive. First, we investigated the influence of the PTQ10:4TIC-4F weight ratio (wt%) in binary conditions. We found that using a wt% of 1:1.5, 1:2 or 1:2.5 give similar PCE close to 8.2% with a FF close to 0.55 (**Table S4**). Then, we fabricated ternary OSCs, with a PTQ10:acceptors wt% of 1:2.5, in which acceptors contains both 4TIC-4F and PC₆₁BM. By varying the 4TIC-4F:PC₆₁BM ratio, we found out that ternary OSCs with 20% to 40% (*i.e.* a PTQ10:PC₆₁BM:4TIC-4F wt% of 1:2:0.5 to 1:1.5:1) of PC₆₁BM gave a similar improved PCE of 9.7% with a FF surpassing 0.64, as shown in **Table 1**. The current density-voltage (*J-V*) curves, the external quantum efficiency (EQE) spectra and the evolution of each photovoltaic parameter depending on the 4TIC-4F:PC₆₁BM wt% with a PTQ10:acceptors wt% of 1:2.5 are shown in **Figure 2**. The same test using a PTQ10:acceptors wt% of 1:2 demonstrated a similar trend to what obtained with a wt% of 1:2.5 (**Table S5**).

Table 1. Photovoltaic parameters and integrated J_{SC} as function of different weight wt% of PC₆₁BM in 4TIC-4F:PC₆₁BM with a PTQ10:acceptors weight wt% of 1:2.5.

PC ₆₁ BM content	V_{oc} [V]	J_{sc} [mA.cm ⁻²]	Integrated J_{sc} [mA.cm ⁻²]	FF	PCE ^{a)} [%]	PCE _{max} [%]
0%	0.77 ± 0.01	19.3 ± 0.1	18.5	0.55 ± 0.01	8.1 ± 0.2	8.4
15%	0.79 ± 0.01	19.4 ± 0.4	18.8	0.61 ± 0.01	9.2 ± 0.2	9.5
20%	0.79 ± 0.01	19.2 ± 0.3	18.5	0.64 ± 0.01	9.7 ± 0.2	9.9
30%	0.80 ± 0.01	18.9 ± 0.2	18.5	0.63 ± 0.01	9.6 ± 0.2	9.9
40%	0.81 ± 0.01	18.6 ± 0.1	18.0	0.64 ± 0.01	9.7 ± 0.1	9.8
50%	0.82 ± 0.01	17.5 ± 0.2	17.3	0.62 ± 0.01	8.9 ± 0.1	9.0
75%	0.86 ± 0.01	12.9 ± 0.1	13.1	0.56 ± 0.01	6.2 ± 0.1	6.3
100%	0.89 ± 0.01	5.7 ± 0.2	5.6	0.67 ± 0.03	3.4 ± 0.1	3.6

a) The standard deviations are based on measurements of eight independent devices

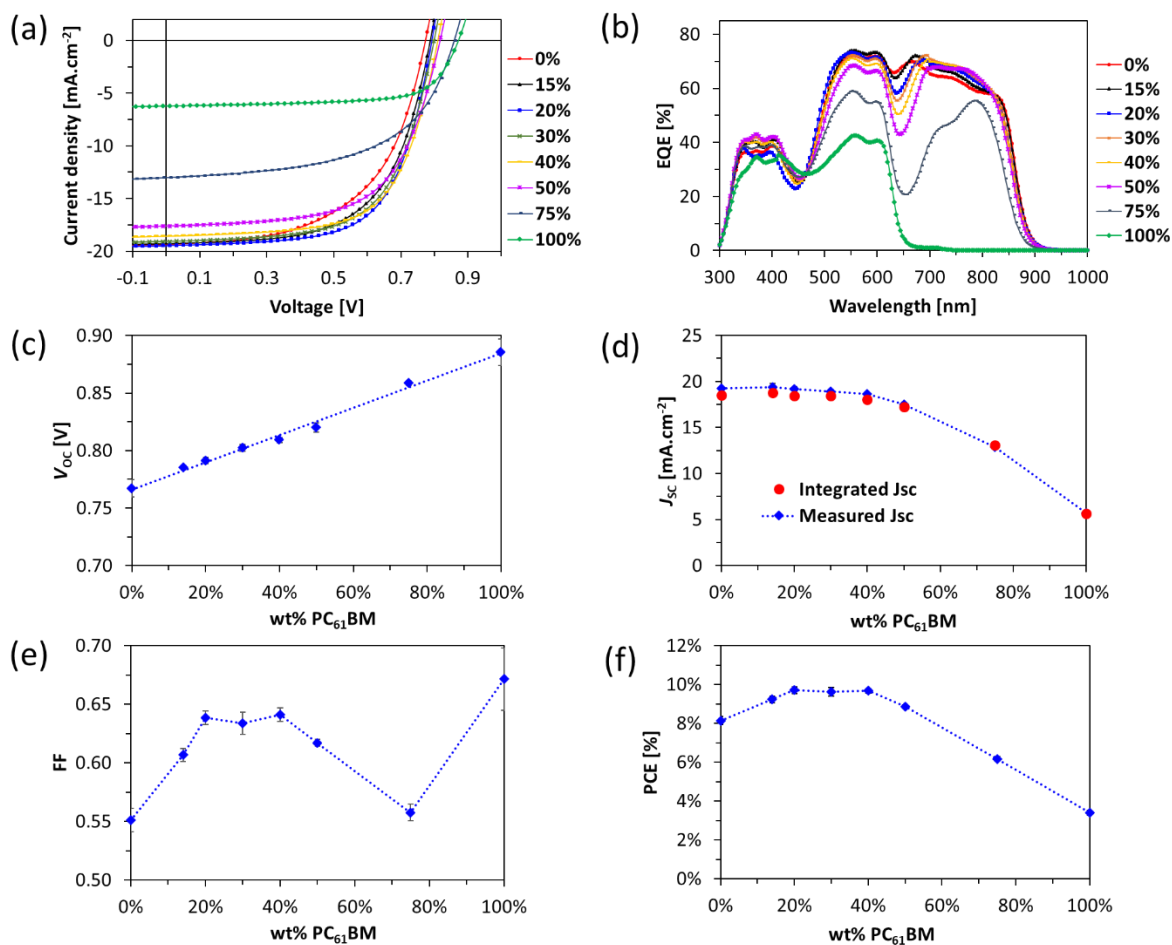


Figure 2. (a) Current density-voltage (J-V) characteristics of optimized binary and ternary OSCs under AM 1.5G solar irradiation (1000 W.cm^{-2}) and (b) corresponding EQE spectra. (c) V_{OC} (d) measured J_{SC} from IV curves, integrated J_{SC} calculated from the EQE spectra (e) FF and (f) PCE as a function of different weight ratios of PC₆₁BM in 4TIC-4F:PC₆₁BM with a PTQ10:acceptors wt% of 1:2.5.

A linear trend between the V_{OC} and the PC₆₁BM wt% is observed. This behavior can be explained by the higher lowest unoccupied molecular orbital (LUMO) energy level of the PC₆₁BM compared to that of 4TIC-4F, resulting in a larger energy offset with the highest unoccupied molecular orbital (HOMO) of the polymeric donor.^[36] This trend suggests the formation of an alloy-like mixed phase between PC₆₁BM and 4TIC-4F.^[37] Morphological analyzes discussed below confirmed this hypothesis. Interestingly, the J_{SC} remains steady when the PC₆₁BM content increases from 0% to 40%. EQE spectra confirmed these values, as illustrated in **Figure 2**. It can be attributed to two main factors: on the one hand, 4TIC-4F is

able to retain a considerable and sufficient absorption, even at low concentrations, due to its high extinction coefficient and relative larger thickness of ~160 nm (see **Figure S2** for the UV-vis spectra of the different blends). On the other hand, adding PC₆₁BM leads to an increased EQE in the wavelength range of 700-850 nm, which compensates the drop at 650 nm and gives a similar J_{SC} .

Interestingly, the FF is the parameter which is most affected by the addition of PC₆₁BM. As the FF is mainly linked to the charge transport, we characterized the electron and hole mobility using the SCLC method. We evaluated and compared the hole and electron mobilities (μ_h and μ_e) of different blend compositions. Hole-only devices were fabricated with the structure of ITO/PEDOT:PSS/active layer/MoO₃/Ag and electron-only devices with the structure of ITO/ZnO/active layer/Ca/Al. The J - V curves of each device were recorded in the dark, which enabled to extract the mobility with the Mott-Gurney law, Equation S3, as described in Supporting Information.^[38] First, we validated this law by measuring μ_h and μ_e of pristine PTQ10 and 4TIC-4F at several layer thicknesses. As shown in **Figure S3**, the extracted μ_h or μ_e remain similar with different active layer thicknesses, validating this model for further studies. The μ_h of pristine PTQ10 was estimated at $1.5 \times 10^{-3} \text{ cm}^2 \cdot \text{V}^{-1} \cdot \text{s}^{-1}$ and the μ_e of pristine 4TIC-4F at $1.0 \times 10^{-3} \text{ cm}^2 \cdot \text{V}^{-1} \cdot \text{s}^{-1}$. This experimental μ_e is consistent with reported values.^[30] For the binary blend PTQ10:4TIC-4F, we found a μ_h of $1.7 \times 10^{-4} \text{ cm}^2 \cdot \text{V}^{-1} \cdot \text{s}^{-1}$ and a μ_e of $6.9 \times 10^{-4} \text{ cm}^2 \cdot \text{V}^{-1} \cdot \text{s}^{-1}$. The hole mobility is decreased by an order of magnitude in the blend, suggesting that the morphology of PTQ10 is disrupted by the 4TIC-4F acceptor. On the contrary, the hole mobility of the binary blend PTQ10:PC₆₁BM ($2.3 \times 10^{-3} \text{ cm}^2 \cdot \text{V}^{-1} \cdot \text{s}^{-1}$) is of the same order of magnitude as the one of pristine PTQ10 ($1.5 \times 10^{-3} \text{ cm}^2 \cdot \text{V}^{-1} \cdot \text{s}^{-1}$), which suggest that the morphology of PTQ10 is not disrupted by the presence of PC₆₁BM. As a result, the electron and hole mobilities are highly unbalanced in the blend PTQ10:4TIC-4F (μ_e/μ_h of 4.2), which can result in low FF.^[39] As a consequence of unbalanced mobilities, charge carriers with

the lowest mobility can build up in the active layer, which could lead to space charge limitation. This creates an electric field able to shield the built-in electric field across the device, which is detrimental to the FF.^[39] As shown in **Table 2**, the progressive addition of PC₆₁BM as a ternary component leads to a μ_e decrease and a μ_h increase, giving rise to a better balance between the hole mobility and the electron mobility. For PC₆₁BM ratio ranging from 10% to 50%, the ratio μ_e/μ_h is close to the unity, which corresponds to the optimal FF in the OSCs, as depicted in **Figure 3**. Thus, improving the mobility balance with the ternary blend strategy appears to be an effective strategy to enhance the FF of solar cells. When more PC₆₁BM is added into the blend, the FF decreases sharply (FF = 0.56 for 75% of PC₆₁BM). This FF drop can be ascribed to trap-assisted recombination, as demonstrated by other studies of ternary blends with such energetic configuration^[26]. Indeed, when a small amount of 4TIC-4F is added in the PTQ10:PC₆₁BM blend, the electrons can be trapped in the 4TIC-4F phase due to its lower LUMO level.

Table 2. Hole and electron mobility calculated with the SCLC method for different PC₆₁BM content in 4TIC-4F:PC₆₁BM with a PTQ10:acceptors ratio of 1:2.5.

PC ₆₁ BM content	$\mu_h^{(a)}$ [cm ² .V ⁻¹ .s ⁻¹]	$\mu_e^{(a)}$ [cm ² .V ⁻¹ .s ⁻¹]	μ_e/μ_h	FF
0%	$1.7 \times 10^{-4} \pm 4.10^{-5}$	$6.9 \times 10^{-4} \pm 8.10^{-5}$	4.2	0.55 ± 0.01
10%	$2.6 \times 10^{-4} \pm 4.10^{-5}$	$3.8 \times 10^{-4} \pm 4.10^{-5}$	1.5	0.61 ± 0.01
20%	$2.6 \times 10^{-4} \pm 5.10^{-5}$	$3.7 \times 10^{-4} \pm 5.10^{-5}$	1.4	0.64 ± 0.01
30%	$3.1 \times 10^{-4} \pm 4.10^{-5}$	$3.3 \times 10^{-4} \pm 4.10^{-5}$	1.0	0.63 ± 0.01
40%	$3.3 \times 10^{-4} \pm 5.10^{-5}$	$2.9 \times 10^{-4} \pm 1.10^{-5}$	0.9	0.64 ± 0.01
50%	$4.4 \times 10^{-4} \pm 6.10^{-5}$	$3.0 \times 10^{-4} \pm 3.10^{-5}$	0.7	0.62 ± 0.01
75%	$4.8 \times 10^{-4} \pm 9.10^{-5}$	$1.5 \times 10^{-4} \pm 2.10^{-5}$	0.3	0.56 ± 0.01
100%	$2.3 \times 10^{-3} \pm 2.10^{-4}$	$7.8 \times 10^{-4} \pm 7.10^{-5}$	0.3	0.67 ± 0.03

a) The standard deviations are based on measurements of eight independent devices

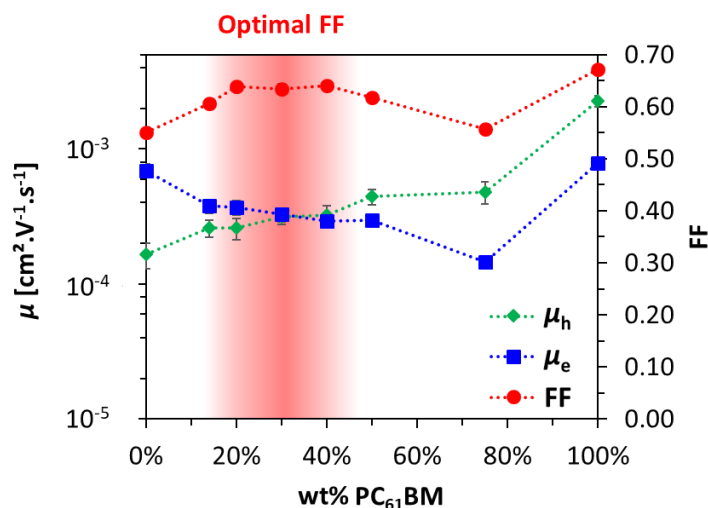


Figure 3. Evolution of electrons and holes mobility (μ_e , μ_h) and fill factor FF as a function of the PC₆₁BM content in 4TIC-4F:PC₆₁BM with a PTQ10:acceptors ratio of 1:2.5.

To elucidate how PC₆₁BM leads to the observed changes in charge transport, GIWAXS characterizations on the active layer were performed. First, we analyzed pristine PTQ10, 4TIC-4F and PC₆₁BM (**Figure S5**). PTQ10 out-of-plane (OOP) profile shows a lamellar diffraction peak at 0.3 \AA^{-1} , a π - π stacking diffraction peak at 1.8 \AA^{-1} and a broader signal at 1.4 \AA^{-1} , in agreement with previous studies.^[15] This indicates that the backbone of PTQ10 is in the plane of the film, but it is otherwise not strongly preferentially orientated, it is likely a 2D powder with a random angular orientation distribution about the backbone axis (For details how such a distribution relates to the observed GI-WAXS pattern, see SI). The absence of higher diffraction orders indicates that ordering is only short range. 4TIC-4F shows a highly ordered and preferentially oriented texture with several peaks between 0.5 and 2 \AA^{-1} . A strong lamellar diffraction peak is present at 0.4 \AA^{-1} in the OOP profile. In both planes, PC₆₁BM shows characteristic peaks at ~ 0.7 , ~ 1.4 and $\sim 2.1 \text{ \AA}^{-1}$, in agreement with previous studies.^[40] We subsequently analyzed the binary and ternary blends (**Figure 4**). In the PTQ10:4TIC-4F binary blend, π - π stacking peaks are identified at 1.8 \AA^{-1} and a (100) peak at 0.3 \AA^{-1} in the OOP profile, which suggests the presence of PTQ10 rich, partially ordered domains with a “rolling log” texture. Besides, the signal of 4TIC-4F is hard to identify in the blend, which indicates that 4TIC-4F becomes less crystalline and disordered when blended with PTQ10. That said, there

is a shoulder peak in the low q range in the OOP profile of the binary (0% PC₆₁BM) and the ternary blend with 15% of PC₆₁BM, which could be attributed to a partially ordered 4TIC-4F phases (0.4 Å⁻¹). In ternary blends, when the PC₆₁BM content increases to 30%, the 4TIC-4F peak at 0.4 Å⁻¹ disappears, suggesting that 4TIC-4F is less ordered and is forming a mixed phase with PC₆₁BM to form an acceptors alloy at wt%PC₆₁BM < 50%.^[37] The decreased structural order and increased electronic disorder in 4TIC-4F:PC₆₁BM phase in the ternary blends can likely explain the lower μ_e for ternary blends as the hopping of the charges might be impeded. The electrons get rapidly trapped in the 4TIC-4F phase on account of its lower LUMO (by 210 meV) and need to travel around the PC₆₁BM molecules or clusters.^[41] The characteristic peak of PC₆₁BM at $q = 0.7 \text{ \AA}^{-1}$ only appears when PC₆₁BM content exceeds 50%, which has identified with phase-segregating PC₆₁BM cluster/domains.^[42] This suggests that in blends containing 0% to 50% PC₆₁BM, PC₆₁BM mixes with the 4TIC-4F domains and possibly with the PTQ10:4TIC-4F mixed amorphous phases. Above 50% of PC₆₁BM content, PC₆₁BM clusters appear, resulting in a more tortuous percolation pathway for the electrons around the PC₆₁BM molecules and clusters. This causes electron traps in the 4TIC-4F phase, until the PC₆₁BM concentration reaches 100% and electron mobility increases greatly. This fully and consistently explains the evolution of the electron mobility with PC₆₁BM content. Correlating the hole mobility in the binary/ternary as a function of PC₆₁BM content with π - π coherence length and intensity of the (010) or texture is stymied by the overlapping of the PTQ10 (010) peaks and the 1.4 and 2.1 Å⁻¹ features of the PC₆₁BM and the weak signature of the PTQ10 (010) peak. Attempts to fit PTQ10 did not reveal any consistent trend outside the margins of errors. The monotonic increase in hole mobility with PC₆₁BM content suggests that 4TIC-4F disrupts the packing or preferential texture of PTQ10 more than PC₆₁BM does. In addition, the hole mobility evolves towards the intrinsic mobility of PTQ10 ($1.5 \times 10^{-3} \text{ cm}^2 \cdot \text{V}^{-1} \cdot \text{s}^{-1}$) for all blends that contain 4TIC-4F, and this then is slight exceeded by the PTQ10:PC₆₁BM binary with a mobility of $2.3 \times 10^{-3} \text{ cm}^2 \cdot \text{V}^{-1} \cdot \text{s}^{-1}$.

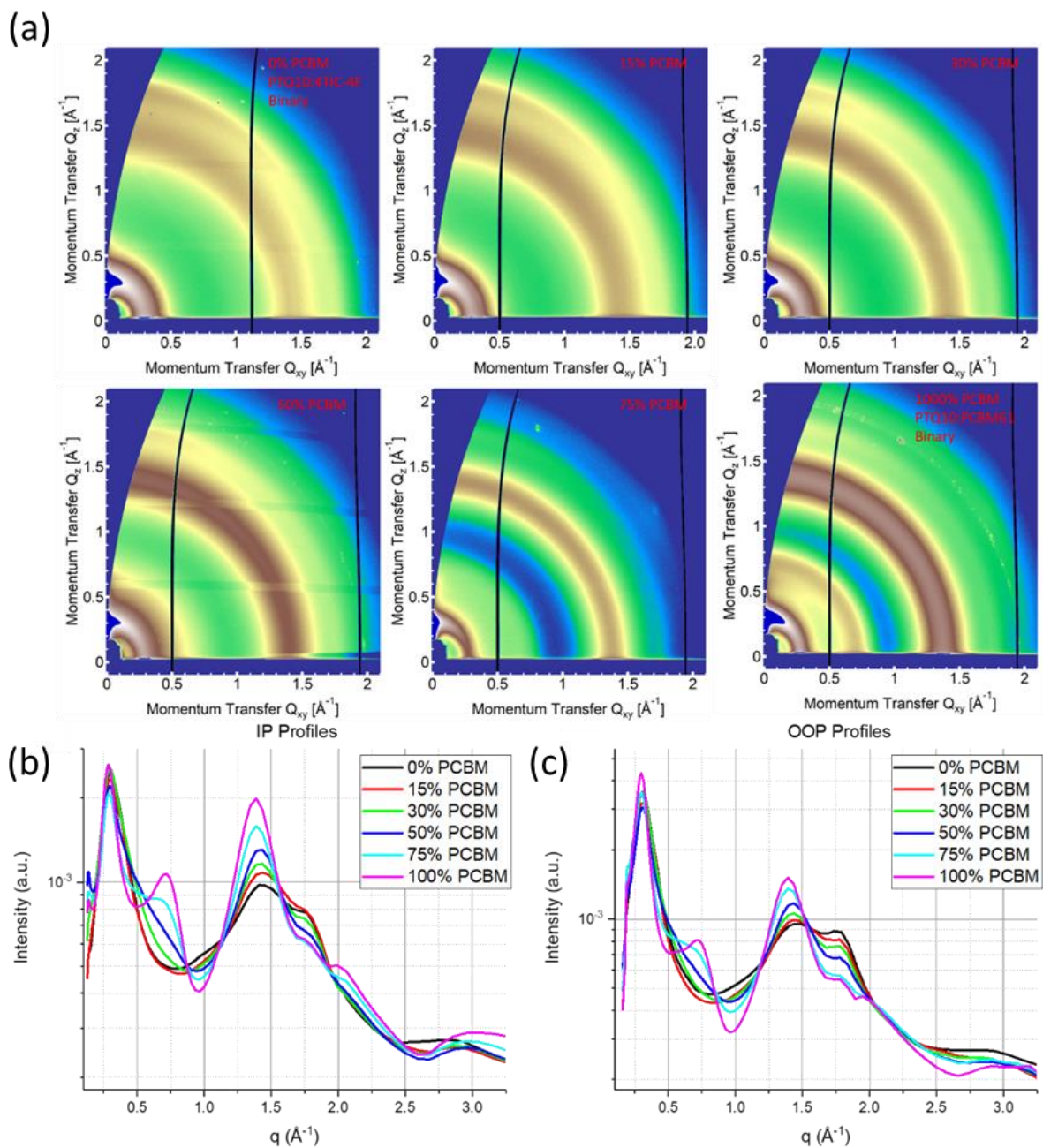


Figure 4. (a) 2D GIWAXS patterns corresponding to the 0%, 15%, 30%, 50%, 75% and 100% PC₆₁BM content samples. (b) Corresponding in plane and (c) out of plane line cuts.

As a complement to GIWAXS analyzes, AFM measurements were performed to characterize the surface of the films. As shown in **Figure S7**, the height images of the binary and the optimal ternary blend are quite similar, which suggest that PC₆₁BM does not alter much the morphology of PTQ10:4TIC-4F, in agreement with GIWAXS interpretations. For the binary blend PTQ10:PC₆₁BM, large domains are observed. These domains could be phase-separated pure PC₆₁BM domains as indicated in the high PC₆₁BM content GIWAXS data. This phase-

separation and change in domain length scale could further explain the low EQE for this blend as well as the high μ_h and μ_e , close to those of pristine PTQ10 and PC₆₁BM.

To elucidate and confirm the different inferred miscibility of each material with each other, we performed contact angle analyzes using water and ethylene glycol (EG) drops on top of each pristine films. These contact angles enabled to derive the surface energy γ of each material via the empiric Wu's method (Equation S4), as described in Supporting Information.^[43] Then, it is possible to calculate the interfacial tension γ_{AB} between two organic semiconductors A and B (Equation S5). This enable to predict the phase separation of the materials when they are mixed together : a low γ_{AB} involves a high miscibility between A and B and a high γ_{AB} involves a poor miscibility between A and B.^[44] Contact angle values, goniometer pictures, calculated surface energies and interfacial tensions are summarized in **Table S6**, **Figure S8** and **Table S7**. The low interfacial tension $\gamma_{4TIC-4F-PC61BM}$ of 2.2 mN.m⁻¹ confirms the partial miscibility between both acceptors in agreement with the presence of a mixed phase of 4TIC-4F and PC₆₁BM in ternary blends with wt%PC₆₁BM < 50% and the linear evolution of the V_{OC} with the PC₆₁BM content. In contrast, the high $\gamma_{PTQ10-PC61BM}$ of 12.7 mN.m⁻¹ means that PTQ10 and PC₆₁BM tend to demix more strongly, which correlates with the SCLC mobility of the binary blend PTQ10:PC₆₁BM and its corresponding AFM image. The interfacial tension of $\gamma_{PTQ10:4TIC-4F}$ of 5.5 mN.m⁻¹ indicates that 4TIC-4F is more miscible in PTQ10 than PC₆₁BM. This scenario is consistent and supportive of the hole mobility inferences made where the 4TIC-4F has a detrimental impact on the ability of PTQ10 to transport holes, whereas PC₆₁BM does not.

3. Towards the industrialization of the ternary blend PTQ10:4TIC-4F:PC₆₁BM

From an industrial point of view, high PCE is not the only constraint to scale up new materials for the active layer of OPV modules. This ternary blend is deposited using TMB, a non-chlorinated solvent, which is one of the main criteria to produce OPV modules by slot-die coating on a large-scale production line. Important to note that no thermal annealing is used,

without any solvent additive, which is a way to reduce the energy footprint of these solar cells. To evaluate the industrial potential of this blend, we investigated the photostability of the encapsulated binary and optimal ternary devices by aging them under light soaking (1000 W.m^{-2} , xenon lamp) with a UV cutoff filter at 380 nm in open circuit ageing conditions. The performances of each device were measured at regular intervals. **Figure 5** shows the normalized PCE data and **Figure S9** shows the evolution of each photovoltaic parameter as function of the light-soaking time. The PCE of the binary blend drop from 8.2% to 5.5% after 200 h of light-soaking, which correspond to a 33% PCE drop. The ternary blend shows an improved photostability: in the same conditions, the PCE drops from 9.3% to 7.5%, which correspond to a 20% PCE drop. Previous works already showed an improved photostability of ternary blends comprising PC₆₁BM or PC₇₁BM as co-acceptor.^{[45][28][46]} Stability is a complex issue though, and the primary reasons for binary device degradations are often related to the overpurification of the mixed domains or crystallization of the acceptor.^{[47][48][49][50]} In this system, PC₆₁BM strongly phase separates from the PTQ10, the mechanism for stabilization would have to be different than countering the overpurification of the mixed domains. Stability is likely related to the crystallization of the NFA and due to the increased entropy of PC₆₁BM:4TIC-4F phases, the PC₆₁BM hinders or prevents the crystallization of 4TIC-4F. Additionally, fullerenes are well-known radical scavengers and they have proven to slow down the degradation of several active layers. Then, the improvement of stability can also be explained by this property of the fullerene derivative.^{[51][52]}

In order to quantify the improved performance-stability-cost balance with this ternary blend strategy, we evaluated its industrial figure of merit (i-FOM) as defined by Min *et al.*^[53] In our study, the i-FOM is based on the PCE after 200 h of light soaking and the synthetic complexity index of the photoactive blend (SC_{Blend}), determined according to the equations (1) and (2), where SC_D , SC_{A1} and SC_{A2} are the SC index of the donor, the first acceptor (4TIC-4F in our case) and the second acceptor (PC₆₁BM in our case), respectively. w_D , w_{A1} and w_{A2} are the wt%

of the donor, the first acceptor and the second acceptor, respectively.

$$i\text{-FOM} = \frac{PCE_{200\text{ h light soaking}}}{SC_{Blend}} \quad (1)$$

$$SC_{Blend} = SC_D \times w_D + SC_{A1} \times w_{A1} + SC_{A2} \times w_{A2} \quad (2)$$

We evaluated the i-FOM of different blend compositions. The SC indexes were evaluated according to organic syntheses available in the literature. The calculations and references are summarized in **Table S2**. We found a SC index of 16.4%, 65.9% and 17.3% for PTQ10, 4TIC-4F and PC₆₁BM, respectively. PC₆₁BM has a lower SC index compared to the NFA 4TIC-4F and improves the initial performances as well as the photostability of the OSCs. Thus, adding PC₆₁BM as a ternary component drastically improves the i-FOM from 0.11 for the binary blend to 0.20 for the optimal ternary blend, as presented in **Table 3** and **Figure 5**.

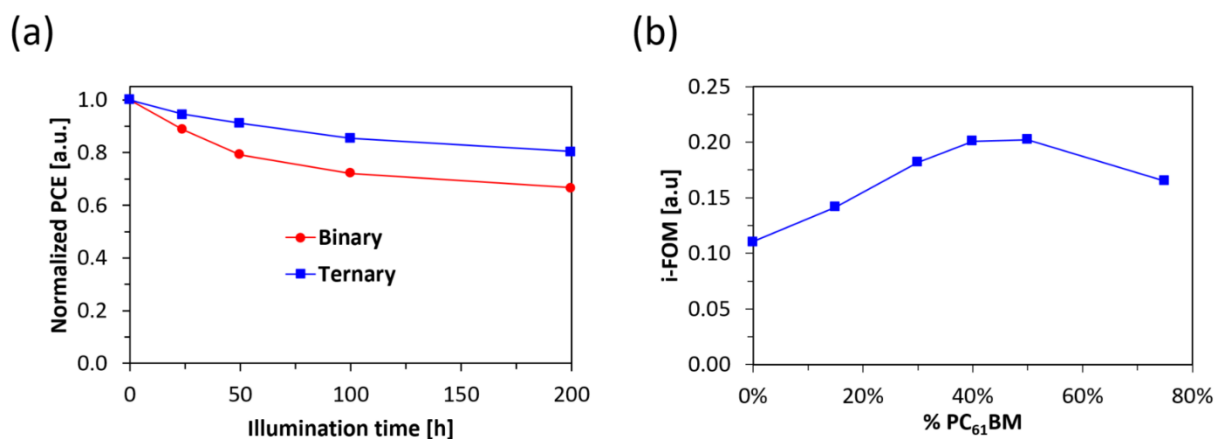


Figure 5. (a) Photostability of the binary and optimal ternary blend under a continuously 1000 W.m⁻² light-soaking (Xenon lamp). (b) The i-FOM evolution in function of the blend composition.

Table 3. The i-FOM calculation of each blend with different PC₆₁BM wt%.

wt%PTQ10	wt%4TIC-4F	wt%PC ₆₁ BM	SC _{Blend} [%]	PCE _{200h light soaking} [%]	i-FOM [a.u.]
33%	67%	0%	49.4	5.47	0.11
33%	57%	10%	44.8	6.35	0.14
33%	47%	20%	40.3	7.33	0.18
33%	40%	27%	37.3	7.49	0.20
33%	33%	33%	34.3	6.92	0.20
33%	17%	50%	26.7	4.41	0.17

Conclusions

In conclusion, we developed a novel ternary blend PTQ10:4TIC-4F:PC₆₁BM yielding a PCE of 9.9% when fabricated using essential industrial constraints: the use of a non-chlorinated solvent without solvent additive, the absence of thermal annealing or solvent vapor annealing, a relatively high active layer thickness of *ca* 160 nm, a sufficient light stability and a promising i-FOM. In particular, adding PC₆₁BM enabled a ~80% increase of the i-FOM, which highlights the benefit of PC₆₁BM as a ternary component towards industrial applications. Compared to the host binary blend, ternary OSCs give higher FF and V_{OC} . SCLC mobility and morphological analyzes suggest that PC₆₁BM enables a better hole and electron mobility balance, which is beneficial for the FF. At low content, PC₆₁BM mixes with 4TIC-4F and with the mixed phase, which decreases the electron mobility. In contrast, the hole mobility is improved: 4TIC-4F is detrimental to the ability of PTQ10 to transport holes, unlike PC₆₁BM. Because PC₆₁BM has a higher LUMO than 4TIC-4F, it has also a beneficial impact on the V_{OC} : the acceptors alloy formed in ternary blends enable to tune it as function of the acceptors ratios. Finally, this contribution shows the industrial potential of the ternary blend strategy in OPV and brings new insights to the role of PC₆₁BM in ternary blend.

Keywords

Polymer solar cells, low-cost semiconducting polymer, non-chlorinated solvent processing, ternary blend, industrial figure of merit

Supporting Information

Supporting Information is available from the Wiley Online Library or from the author.

Acknowledgments

The authors thank the ANRT (CIFRE grant N° 2017/0620) for doctoral scholarship of R. Szymanski at ARMOR SOLAR POWER FILMS and IMS laboratory. The authors thank also

Julien Hunel (ISM laboratory) for the AFM microscopy made in the analytical platform SIV from the ISM, Gilles Roche (IMS) for relevant discussions on the synthetic complexity index determination and Lionel Hirsch (IMS) for relevant discussions on the physics of OSCs. R. Henry was supported by the National Science Foundation (NSF, INFEWS, CBET, award number 1639429). X-ray data were taken at beamline 7.3.3 at the Advanced Light Source, which is supported by the Director, Office of Basic Energy Science, of the U.S. Department of Energy under contract no. DE-AC02-05CH11231.

Received: ((will be filled in by the editorial staff))

Revised: ((will be filled in by the editorial staff))

Published online: ((will be filled in by the editorial staff))

References

- [1] Z. Li, C.-C. Chueh, A. K. Y. Jen, *Prog. Polym. Sci.* **2019**, *99*, 101175.
- [2] Y. Xu, H. Yao, J. Hou, *Chinese J. Chem.* **2019**, *37*, 207.
- [3] P. Cheng, G. Li, X. Zhan, Y. Yang, *Nat. Photonics* **2018**, *12*, 131.
- [4] Q. Liu, Y. Jiang, K. Jin, J. Qin, J. Xu, W. Li, J. Xiong, J. Liu, Z. Xiao, K. Sun, S. Yang, X. Zhang, L. Ding, *Sci. Bull.* **2020**, *65*, 272.
- [5] J. Yuan, Y. Zhang, L. Zhou, G. Zhang, H. L. Yip, T. K. Lau, X. Lu, C. Zhu, H. Peng, P. A. Johnson, M. Leclerc, Y. Cao, J. Ulanski, Y. Li, Y. Zou, *Joule* **2019**, *3*, 1140.
- [6] B. Fan, D. Zhang, M. Li, W. Zhong, Z. Zeng, L. Ying, F. Huang, Y. Cao, *Sci. China Chem.* **2019**, *62*, 746.
- [7] D. Li, X. Chen, J. Cai, W. Li, M. Chen, Y. Mao, B. Du, J. A. Smith, R. C. Kilbride, M. E. O’Kane, X. Zhang, Y. Zhuang, P. Wang, H. Wang, D. Liu, R. A. L. Jones, D. G. Lidzey, T. Wang, *Sci. China Chem.* **2020**, *1*.
- [8] Z. Zheng, H. Yao, L. Ye, Y. Xu, S. Zhang, J. Hou, *Mater. Today* **2020**, *35*, 115.
- [9] D. Qian, L. Ye, M. Zhang, Y. Liang, L. Li, Y. Huang, X. Guo, S. Zhang, Z. Tan, J.

- Hou, *Macromolecules* **2012**, *45*, 9611.
- [10] M. Zhang, X. Guo, W. Ma, H. Ade, J. Hou, *Adv. Mater.* **2015**, *27*, 4655.
- [11] S. H. Liao, H. J. Jhuo, Y. S. Cheng, S. A. Chen, *Adv. Mater.* **2013**, *25*, 4766.
- [12] S. C. Price, A. C. Stuart, L. Yang, H. Zhou, W. You, *J. Am. Chem. Soc.* **2011**, *133*, 4625.
- [13] H. Bin, L. Gao, Z.-G. Zhang, Y. Yang, Y. Zhang, C. Zhang, S. Chen, L. Xue, C. Yang, M. Xiao, Y. Li, *Nat. Commun.* **2016**, *7*, 13651.
- [14] C. L. Chochos, M. Spanos, A. Katsouras, E. Tatsi, S. Drakopoulou, V. G. Gregoriou, A. Avgeropoulos, *Prog. Polym. Sci.* **2019**, *91*, 51.
- [15] C. Sun, F. Pan, H. Bin, J. Zhang, L. Xue, B. Qiu, Z. Wei, Z.-G. Zhang, Y. Li, *Nat. Commun.* **2018**, *9*, 743.
- [16] Y. Wu, Y. Zheng, H. Yang, C. Sun, Y. Dong, C. Cui, H. Yan, Y. Li, *Sci. China Chem.* **2020**, *63*, 265.
- [17] R. Po, G. Bianchi, C. Carbonera, A. Pellegrino, *Macromolecules* **2015**, *48*, 453.
- [18] D. Yuan, F. Pan, L. Zhang, H. Jiang, M. Chen, W. Tang, G. Qin, Y. Cao, J. Chen, *Sol. RRL* **2020**, 2000062.
- [19] X. Li, F. Pan, C. Sun, M. Zhang, Z. Wang, J. Du, J. Wang, M. Xiao, L. Xue, Z.-G. G. Zhang, C. Zhang, F. Liu, Y. Li, *Nat. Commun.* **2019**, *10*, 519.
- [20] X. Li, J. Yao, I. Angunawela, C. Sun, L. Xue, A. Liebman-Pelaez, C. Zhu, C. Yang, Z. G. Zhang, H. Ade, Y. Li, *Adv. Energy Mater.* **2018**, *8*, 1800815.
- [21] Z. Luo, C. Sun, S. Chen, Z. G. Zhang, K. Wu, B. Qiu, C. Yang, Y. Li, C. Yang, *Adv. Energy Mater.* **2018**, *8*, 1800856.
- [22] W. Xu, F. Gao, *Mater. Horizons* **2018**, *5*, 206.
- [23] B. Guo, W. Li, X. Guo, X. Meng, W. Ma, M. Zhang, Y. Li, *Adv. Mater.* **2017**, *29*,

1702291.

- [24] C. Yang, Y. Sun, Q. Li, K. Liu, X. Xue, Y. Huang, K. Ren, L. Li, Y. Chen, Z. Z. Wang, S. Qu, Z. Z. Wang, *J. Phys. Chem. Lett.* **2020**, *11*, 927.
- [25] J. Wang, J. Wang, F. Zhang, *Org. Electron.* **2019**, *67*, 253.
- [26] R. Yu, H. Yao, Y. Cui, L. Hong, C. He, J. Hou, *Adv. Mater.* **2019**, *31*, 1902302.
- [27] W. Li, D. Yan, F. Liu, T. Russell, C. Zhan, J. Yao, *Sci. China Chem.* **2018**, *61*, 1609.
- [28] Q. Zhao, Z. Xiao, J. Qu, L. Liu, H. Richter, W. Chen, L. Han, M. Wang, J. Zheng, Z. Xie, L. Ding, F. He, *ACS Energy Lett.* **2019**, *4*, 1106.
- [29] S. Dai, T. Li, W. Wang, Y. Xiao, T. K. Lau, Z. Li, K. Liu, X. Lu, X. Zhan, *Adv. Mater.* **2018**, *30*, 1706571.
- [30] X. Shi, X. Liao, K. Gao, L. Zuo, J. Chen, J. Zhao, F. Liu, Y. Chen, A. K. Y. Jen, *Adv. Funct. Mater.* **2018**, *28*, 1802324.
- [31] J. Zhao, Y. Li, G. Yang, K. Jiang, H. Lin, H. Ade, W. Ma, H. Yan, *Nat. Energy* **2016**, *1*, 15027.
- [32] J. C. Hummelen, B. W. Knight, F. Lepeq, F. Wudl, J. Yao, C. L. Wilkins, *J. Org. Chem.* **1995**, *60*, 532.
- [33] D. Baran, R. S. Ashraf, D. A. Hanifi, M. Abdelsamie, N. Gasparini, J. A. Röhr, S. Holliday, A. Wadsworth, S. Lockett, M. Neophytou, C. J. M. Emmott, J. Nelson, C. J. Brabec, A. Amassian, A. Salleo, T. Kirchartz, J. R. Durrant, I. McCulloch, *Nat. Mater.* **2017**, *16*, 363.
- [34] Y. Lin, J. Wang, Z.-G. Zhang, H. Bai, Y. Li, D. Zhu, X. Zhan, *Adv. Mater.* **2015**, *27*, 1170.
- [35] D. F. Swinehart, *J. Chem. Educ.* **1962**, *39*, 333.
- [36] P. P. Khlyabich, B. Burkhart, B. C. Thompson, *J. Am. Chem. Soc.* **2012**, *134*, 9074.

- [37] P. P. Khlyabich, A. E. Rudenko, B. C. Thompson, Y. L. Loo, *Adv. Funct. Mater.* **2015**, *25*, 5557.
- [38] P. N. Murgatroyd, *J. Phys. D. Appl. Phys.* **1970**, *3*, 151.
- [39] J. A. Bartelt, D. Lam, T. M. Burke, S. M. Sweetnam, M. D. McGehee, *Adv. Energy Mater.* **2015**, *5*, 1500577.
- [40] T. Y. Huang, H. Yan, M. Abdelsamie, V. Savikhin, S. A. Schneider, N. A. Ran, T. Q. Nguyen, G. C. Bazan, M. F. Toney, *RSC Adv.* **2019**, *9*, 4106.
- [41] M. Ghasemi, L. Ye, Q. Zhang, L. Yan, J.-H. Kim, O. Awartani, W. You, A. Gadisa, H. Ade, *Adv. Mater.* **2017**, *29*, 1604603.
- [42] J. R. Tumbleston, L. Yang, W. You, H. Ade, *Polymer (Guildf)*. **2014**, *55*, 4884.
- [43] S. Wu, *J. Polym. Sci. Part C Polym. Symp.* **1971**, *34*, 19.
- [44] K. Jiang, G. Zhang, G. Yang, J. Zhang, Z. Li, T. Ma, H. Hu, W. Ma, H. Ade, H. Yan, *Adv. Energy Mater.* **2018**, *8*, 1701370.
- [45] H. Shi, R. Xia, G. Zhang, H.-L. Yip, Y. Cao, *Adv. Energy Mater.* **2019**, *9*, 1803438.
- [46] Y. Zhu, A. Gadisa, Z. Peng, M. Ghasemi, L. Ye, Z. Xu, S. Zhao, H. Ade, *Adv. Energy Mater.* **2019**, *9*, 1900376.
- [47] N. Li, J. D. Perea, T. Kassar, M. Richter, T. Heumueller, G. J. Matt, Y. Hou, N. S. Güldal, H. Chen, S. Chen, S. Langner, M. Berlinghof, T. Unruh, C. J. Brabec, *Nat. Commun.* **2017**, *8*, 14541.
- [48] M. Ghasemi, H. Hu, Z. Peng, J. J. Rech, I. Angunawela, J. H. Carpenter, S. J. Stuard, A. Wadsworth, I. McCulloch, W. You, H. Ade, *Joule* **2019**, *3*, 1328.
- [49] L. Ye, S. Li, X. Liu, S. Zhang, M. Ghasemi, Y. Xiong, J. Hou, H. Ade, *Joule* **2019**, *3*, 443.
- [50] L. Ye, B. A. Collins, X. Jiao, J. Zhao, H. Yan, H. Ade, *Adv. Energy Mater.* **2018**, *8*,

1703058.

- [51] S. Chambon, A. Rivaton, J. L. Gardette, M. Firon, *Sol. Energy Mater. Sol. Cells* **2007**, *91*, 394.
- [52] M. Manceau, S. Chambon, A. Rivaton, J. L. Gardette, S. Guillerez, N. Lematre, *Sol. Energy Mater. Sol. Cells* **2010**, *94*, 1572.
- [53] J. Min, Y. N. Luponosov, C. Cui, B. Kan, H. Chen, X. Wan, Y. Chen, S. A. Ponomarenko, Y. Li, C. J. Brabec, *Adv. Energy Mater.* **2017**, *7*, 1700465.

Copyright WILEY-VCH Verlag GmbH & Co. KGaA, 69469 Weinheim, Germany, 2018.

Supporting Information

Balanced charge transport optimizes industry-relevant ternary polymer solar cells

Robin Szymanski, Reece Henry, Samuel Stuard, Uyxing Vongsaysy, Stéphanie Courtel, Luc Vellutini, Mélanie Bertrand, Harald Ade^{}, Sylvain Chambon, Guillaume Wantz^{*}*

Table S1. Full names of the polymers mentioned in this article.

Abbreviation	Full name
PEDOT:PSS	Poly(3,4-ethylenedioxythiophene) polystyrene sulfonate
PTQ10	Poly[(thiophene)-alt-(6,7-difluoro-2-(2-hexyldecyloxy)quinoxaline)]
PBDB-T	Poly[(2,6-(4,8-bis(5-(2-ethylhexyl)thiophen-2-yl)-benzo[1,2-b:4,5-b']dithiophene))-alt-(5,5-(1',3'-di-2-thienyl-5',7'-bis(2-ethylhexyl)benzo[1',2'-c:4',5'-c']dithiophene-4,8-dione)))]
PBDB-TF (PM6/PBDB-T-2F)	Poly[(2,6-(4,8-bis(5-(2-ethylhexyl-3-fluoro)thiophen-2-yl)-benzo[1,2-b:4,5-b']dithiophene))-alt-(5,5-(1',3'-di-2-thienyl-5',7'-bis(2-ethylhexyl)benzo[1',2'-c:4',5'-c']dithiophene-4,8-dione)))]
PTB7-Th	Poly[[4,8-bis[5-(2-ethylhexyl)-2-thienyl]benzo[1,2-b:4,5-b']dithiophene-2,6-diyl][2-[[2-ethylhexyl)oxy]carbonyl]-3-fluorothieno[3,4-b]thiophenediyl]]
FTAZ	Poly[[4,8-bis[(2-butyldecyl)oxy]benzo[1,2-b:4,5-b']dithiophene-2,6-diyl]-alt-dithienyl-alt-(difluorobenzotriazole)-2-(2-butyldecyl)-5,6-difluoro-2H-benzo[d][1,2,3]triazole]
J71	Poly[[5,6-difluoro-2-(2-hexyldecyl)-2H-benzotriazole-4,7-diyl]-2,5-thiophenediyl[4,8-bis[5-(tripropylsilyl)-2-thienyl]benzo[1,2-b:4,5-b']dithiophene-2,6-diyl]-2,5-thiophenediyl]
D18	Poly[(2,6-(4,8-bis(5-(2-ethylhexyl-3-fluoro)thiophen-2-yl)-benzo[1,2-b:4,5-b']dithiophene))-alt-(dithieno[3',2':3,4;2'',3'':5,6]benzo[1,2-c][1,2,5]thiadiazole)]

Materials

PTQ10, 4TIC-4F and PC₆₁BM were purchased from 1-Materials Inc, PEDOT:PSS from

Heraeus and the MoO₃ powder from NEYCO. The other materials and solvents were common commercial level and used as received from Sigma-Aldrich.

OSC fabrication and characterization

All the OSC devices were fabricated and characterized using an inverted architecture glass/ITO/ZnO/ active layer/MoO₃/Ag, where ZnO and MoO₃ were used as electron transport and hole transport interlayer, respectively. The ITO covered glasses (1.5 cm², 10 Ω², VisionTek) were cleaned by sequential ultrasonic treatments: diluted soap Hellmanex™ III, ultrapure water and isopropanol. The ZnO precursor solution was prepared by mixing zinc acetate dihydrate (165 mg) and ethanolamine (90 μL) with ultrapure ethanol (5 mL). The solution was then stirred at 55 °C in air for 30 min and left at room temperature under continuous stirring until final use. Before depositing the ZnO precursor solution, the substrates were dried and treated by UV-ozone for 15 minutes. After that, ZnO precursor solution was spin-coated to form 30 nm thin films. The substrates were then thermal annealed in air at 180 °C for 30 min. The active layer blends based on different PC₆₁BM ratios were dissolved in TMB at a total weight concentration of 34 mg.mL⁻¹ and stirred overnight at 70 °C in a nitrogen-filled glovebox. The active layers were spin coated on ZnO-covered substrates with a rotation speed of 750 RPM to yield ~160 nm thick films. Afterwards, hole transport layer MoO₃ (7 nm thick with a rate of 0.5 Å.s⁻¹) and electrode Ag (70 nm thick with a rate of 0.5 Å.s⁻¹ for the ten first nanometers, then 2.5 Å.s⁻¹) were formed via vacuum evaporation under a pressure of approximately 10⁻⁶ mbar. The OSCs area was 10.5 mm². Finally, they were encapsulated with a glass cover slip using a UV epoxy glue (Delo-Katiobond LP655) and characterized in air with a 4011A solar simulator from Newport Co (Xenon lamp). The light intensity of the lamp was set at 1-Sun using a calibrated silicon reference cell from Newport Co. Before measuring the OSCs, they were left for at least 1 minute in light to photo-activate the ZnO. The *J-V* curves were recorded in dark and in light using a LabVIEW-controlled Keithley 2400 SMU. EQE measurements were carried out using

a PVE300 Photovoltaic EQE from Bentham Co.

Active layer characterization: UV-vis, thickness, GIWAXS, AFM and contact angle

The substrates used for the characterization are cleaned and treated with UV-ozone with the same procedure used for OSCs fabrication.

The films used to record UV-vis spectra are deposited on quartz substrates by spin coating with the same speed and concentration as the BHJ active layers in OSCs devices. Pristine PTQ10 was dissolved at 12 mg.mL^{-1} and stirred at $70 \text{ }^{\circ}\text{C}$ overnight before its deposition at 800 RPM. Pristine acceptors were deposited by spin-coating at 2000 RPM from a chloroform solution at 8 mg.mL^{-1} previously stirred at room temperature. The spectrophotometer SAFAS UVMC 2 was used to record spectra.

To control the thickness of the active layer of OSCs devices, ZnO was first deposited on glass slides following by the active layer. The procedures were the same as those described for OSCs devices. Each sample was scratched and the thicknesses of the layers were measured with a mechanical profilometer Apha step IQ from KLA-Tencor.

To record the contact angle of each pristine material, a ZnO layer was first deposited on a glass substrate with the same procedure used for OSCs fabrication. Then, each organic semiconductor was spin-coated on top of the ZnO layer from their TMB solution. The solutions were concentrated at 12 mg.mL^{-1} and stirred at $70 \text{ }^{\circ}\text{C}$ overnight. The contact angle measurements were performed using the Krüss DSA100 goniometer. The two test liquids were deionized water and ethylene glycol (Aldrich 99%).

The AFM microscope used in this study was the Dimension Icon from Brücker Co., available in the analytical platform SIV from the ISM laboratory. Tapping mode was used to record the height images. The aspect ratio was equal to 1 and the scan frequency was set at 0.15 Hz. The tip was in silicon-nitride with a measured resonance frequency of 80.5 kHz.

For GIWAXS analyses, each film was deposited on Si/SiO₂ substrates. The measurement took place at the Advanced Light Source at Lawrence Berkeley National Lab, Berkeley, California at beamline 7.3.3 under a helium atmosphere and standard temperature.^[S1] Samples were irradiated using 10 keV hard x-rays at the critical angle of 0.13° for 30 seconds. Beam centering was performed and sample-detector distance was determined to be roughly 275 cm by calibration using silver behenate powder. For pristine 4TIC-4F and PC₆₁BM, an extra ZnO layer was first deposited in order to get a homogenous film. Each material was dissolved in a TMB solution at 12 mg.mL⁻¹ and stirred at 70 °C overnight.

In a 2D powder, the polymer backbones are restricted to be in a plane parallel to the substrate with a random angular distribution. At the same time, the material has a random distribution of the pi-pi and lamella stacking directions. In the in-plane scattering geometry, only those π - π and lamella stacks with backbone orientation that fulfill diffraction conditions are recorded. In the out-of-plane direction, all π - π and lamella stacks with out-of-plane orientation are recorded for all backbone orientations. To account for the missing populations that don't fulfill the scattering conditions, a correction factor of $\sin(\chi)$ is required, where χ is the azimuthal angle relative to q_z axis. Because of the undetected populations, the raw data of a 2D powder will have a (100) and (010) signal intensity proportional to $1/\sin(\chi)$, giving the illusion that the in-plane populations are low when in fact the in-plane and out-of-plane stacking probabilities are equal. This can lead to the misconception of simultaneous “face-on” and “edge-on” texture, if the $\sin(\chi)$ correction and overall symmetry is not accounted for. For further information and details we refer reader to the website:

http://gisaxs.com/index.php/Example:P3HT_orientation_analysis.

Molar extinction coefficient calculation

To determine the molar extinction coefficient of the used semiconductors, the Beer-Lambert law was used (Equation S1), where A is the measured absorbance [a.u.], ϵ the molar extinction

coefficient [$M^{-1}.cm^{-1}$], l the cuvette length [cm] and c the molar concentration [$mol.L^{-1}$].

$$A = \varepsilon.l.c$$

Equation S1. Beer-Lambert law.

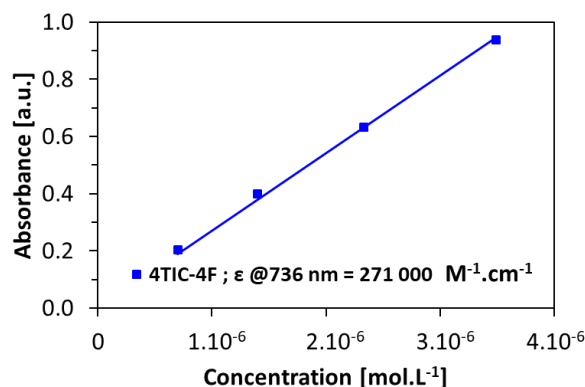


Figure S1. Determination of the molar extinction coefficient of 4TIC-4F using the Beer-Lambert law in TMB solution.

The spectra were recorded with the spectrophotometer SAFAS UVmc1 using a quartz cuvette.

SCLC devices fabrication and characterization

For both hole and electron only devices, the ITO covered glasses were cleaned with the same procedure as the OSCs. For hole only devices, a structure of ITO/PEDOT:PSS/active layer/ MoO_3 /Ag was used. After a 15 minutes UV-ozone treatment, the PEDOT:PSS was spin-coated on it to form a 30 nm thin film. The substrates were subsequently dried at 120 °C for 10 min. After depositing the active layer with the same procedure than the OSCs, MoO_3 and Ag were evaporated in the same conditions than the OSCs. For electron only devices, a structure of ITO/ ZnO /active layer/Ca/Al was used. The ZnO and the active layer were deposited in the same way than for the OSCs. The Ca and Al layers were then thermally evaporated under a pressure of approximately 10^{-6} mbar. The 30 nm thick Ca layer was evaporated with a rate of $0.5 \text{ \AA}.s^{-1}$ and the Al layer was evaporated with a rate of $5 \text{ \AA}.s^{-1}$. Before measuring the electron only devices, they were left for at least 1 minute under a solar simulator in order to photo-activate the ZnO . The J - V curves were recorded in dark using a LabVIEW-controlled Keithley

2400 SMU. Once the J - V curves are recorded, the active layer thickness of each device was systematically measured.

Complementary results

SC determination and values

The SC were determined according Po *et al.* definition (Equation S2^[S2]), where:

- NSS is the number of synthetic steps
- RY is the reciprocal yield (*i.e.* the inverse of the synthetic yield)
- NUO is the number of unit operations including extraction, quenching, recrystallization, distillation, sublimation and excluding filtrations, precipitations and leaching
- NCC is the number of column chromatographies
- NHC is the number of hazardous chemicals used in the total organic synthesis excluding the chemicals used for the purification and characterizations. The H risk considered are those according to CLP regulation 1272/2008/EC. Chemicals are counted as many times as the number of their H risk phrases

$$SC = 35 \frac{NSS}{NSS_{max}} + 25 \frac{\log(RY)}{\log(RY_{max})} + 15 \frac{NUO}{NUO_{max}} + 15 \frac{NCC}{NCC_{max}} + 10 \frac{NHC}{NHC_{max}}$$

Equation S2. Calculation of the SC of an organic semiconductor.

For the polymers, the maximum values for the normalization were defined according to Chochos *et al.* study.^[S3] For the molecular acceptors, the maximum values were fixed according to two NFAs with a complex organic synthesis (Y6 and ID-4F).^{[S4][S5]} **Table S2** shows the value of the SC of some organic semiconductor and the detailed NSS, RY, NUO, NCC and NHC values.

Table S2. SC index of different organic semiconductors mentioned in this study calculated from the NSS, RY, NUO, NCC and NHC values.

Material	NSS	RY	NCC	NUO	NHC	SC index [%]	References
4TIC-4F	13	4.40	7	16	47	65.9	[S7][S8][S9]
PC₆₁BM	4	1.90	2	0	8	17.3	[S10][S11]
Y6	17	25.00	6	29	30	86.9	[S5]
ID4F	15	48.31	9	24	32	89.8	[S4]
<i>Maximum values for the data normalization of acceptors</i>	17	48.31	9	29	49	/	/
PTQ10	4	2.33	1	6	8	16.4	[S5]
J71	9	5.01	5	18	15	42.1	[S5]
PTB7-Th	17	12.20	6	22	43	68.4	[S3]
PBDB-T	12	5.30	6	25	20	53.8	[S5]
PM6	16	32.60	7	26	40	73.3	[S3]
<i>Maximum values for the data normalization of polymers</i>	20	1043	9	29	52	/	[S3]

Table S3. Summary of the photophysical and electrochemical properties of the used materials in this work.

Material	$\lambda_{\max}^{\text{sol}}$ (nm)	$\lambda_{\max}^{\text{film}}$ (nm)	$\lambda_{\text{edge}}^{\text{film}}$ (nm)	HOMO (eV)	LUMO (eV)	E_g^{EC} (eV)	E_g^{OPT} (eV)
PTQ10	561	600	650	-5.54 ^[15]	-2.98 ^[15]	2.56	1.91 ^[S12]
4TIC-4F	734	804	905	-5.60 ^[29]	-4.21 ^[29]	1.39	1.37 ^[S13]
PC ₆₁ BM	332	336	420	-6.05 ^[33]	-4.00 ^[33]	1.95	1.70 ^[S14]

Table S4. Photovoltaic performances of PTQ10:4TIC-4F with different donor:acceptor composition.

PTQ10:4TIC-4F	V_{oc} [V]	J_{sc} [mA.cm ⁻²]	FF	PCE [%]	PCE _{max} [%]
1:1	0.77 ± 0.01	19.6 ± 0.1	0.51 ± 0.01	7.6 ± 0.1	7.7
1:1.5	0.76 ± 0.01	20.3 ± 0.2	0.55 ± 0.01	8.4 ± 0.2	8.6
1:2	0.76 ± 0.01	19.6 ± 0.2	0.54 ± 0.02	8.0 ± 0.2	8.3
1:2.5	0.77 ± 0.01	19.3 ± 0.1	0.55 ± 0.01	8.1 ± 0.2	8.4

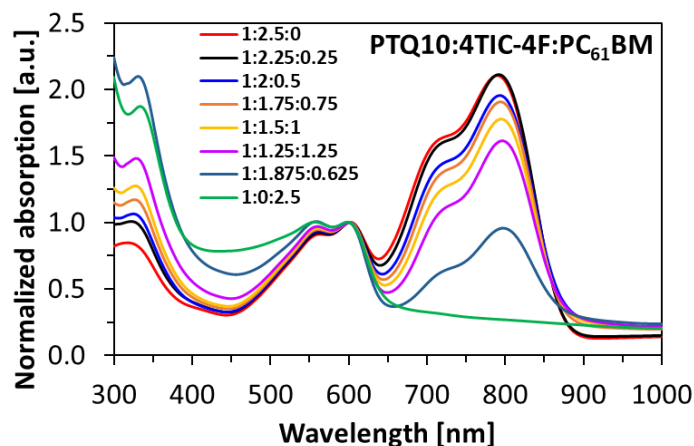


Figure S2. Normalized absorption at 600 nm of PTQ10:4TIC-4F:PC₆₁BM with different wt% of 4TIC-4F:PC₆₁BM.

Table S5. Photovoltaic parameters as function of different weight ratios of PC₆₁BM in 4TIC-4F:PC₆₁BM in the ternary blend PTQ10:4TIC-4F:PC₆₁BM with a donor:acceptors ratio of 1:2.

PC ₆₁ BM content	V _{oc} [V]	J _{sc} [mA.cm ⁻²]	FF	PCE [%]	PCE _{max} [%]
0%	0.76 ± 0.01	19.8 ± 0.2	0.54 ± 0.01	8.0 ± 0.2	8.3
10%	0.77 ± 0.00	20.0 ± 0.3	0.56 ± 0.01	8.6 ± 0.2	9.0
20%	0.78 ± 0.00	20.1 ± 0.1	0.60 ± 0.01	9.4 ± 0.2	9.7
30%	0.79 ± 0.00	20.1 ± 0.5	0.60 ± 0.01	9.5 ± 0.2	10.0
40%	0.80 ± 0.00	19.2 ± 0.2	0.62 ± 0.01	9.5 ± 0.1	9.7
50%	0.81 ± 0.00	18.4 ± 0.1	0.58 ± 0.01	8.6 ± 0.1	8.8
75%	0.84 ± 0.00	13.5 ± 0.1	0.47 ± 0.01	5.3 ± 0.1	5.4
100%	0.89 ± 0.01	5.7 ± 0.2	0.67 ± 0.03	3.4 ± 0.1	3.6

Mott-Gurney model validation for mobility measurement with the SCLC method

For both hole and electron only devices, the Mott-Gurney model, Equation S3, was used.

$$J_{SCLC} = \frac{9}{8} \varepsilon_o \varepsilon_r \mu_o \frac{V^2}{L^3}$$

Equation S3. The Mott-Gurney law

In this equation, ε_r is the relative dielectric constant and was assumed to be 3^[S15], ε_o is the vacuum permeability ($8.854 \cdot 10^{-12}$ F.m⁻¹), μ_o is the mobility in the SCLC regime, V is the applied voltage, and L is the active layer thickness. The transition from ohmic to SCLC behavior can be seen in the transition from a linear J - V trend to a quadratic dependence. First, this model was validated: the hole mobility of the single PTQ10 donor was calculated with different thicknesses

using the device architecture of ITO/PEDOT:PSS/active layer/MoO₃/Ag. The same reasoning was applied for electron only devices with the NFA 4TIC-4F using the device architecture of ITO/ZnO/active layer/Ca/Al.

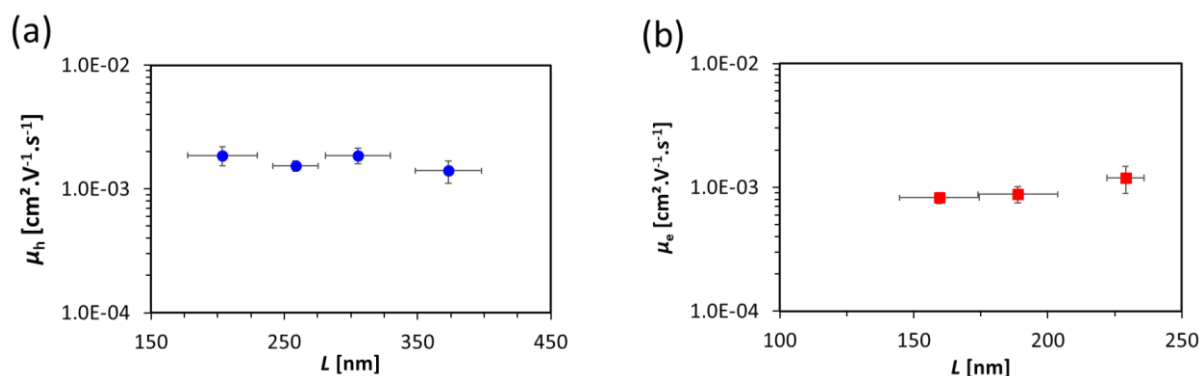


Figure S3. (a) Hole mobility of pristine PTQ10 and (b) electron mobility of pristine 4TIC-4F measured at different active layers thicknesses.

***I-V* curves analyzes of hole only and electron only devices**

Figure S4 shows the *I-V* curves of hole only and electron only devices used to extract hole and electron mobilities of active layer with different PC₆₁BM contents in 4TIC-4F:PC₆₁BM with a PTQ10:acceptors ratio of 1:2.5. For hole only devices, only the positive part of the the *I-V* curves was used. The current in the negative part, which correspond to the charges extracted by the PEDOT:PSS layer, was very low. This is ascribed to a high difference between the work function of PEDOT:PSS (~-5.2 eV) and the HOMO of PTQ10 (-5.55 eV). The symmetry of the curves is better for electron only devices, except for the binary blend PTQ10:PC₆₁BM, in which the mobility was extracted in the negative part of the *I-V* curves. To extract the mobility value, a fit between the Mott-Gurney law and the curve in the SCLC regime was applied. The quadratic sum between the *I-V* curves of the model and the experimental data was below 0.05 mA.

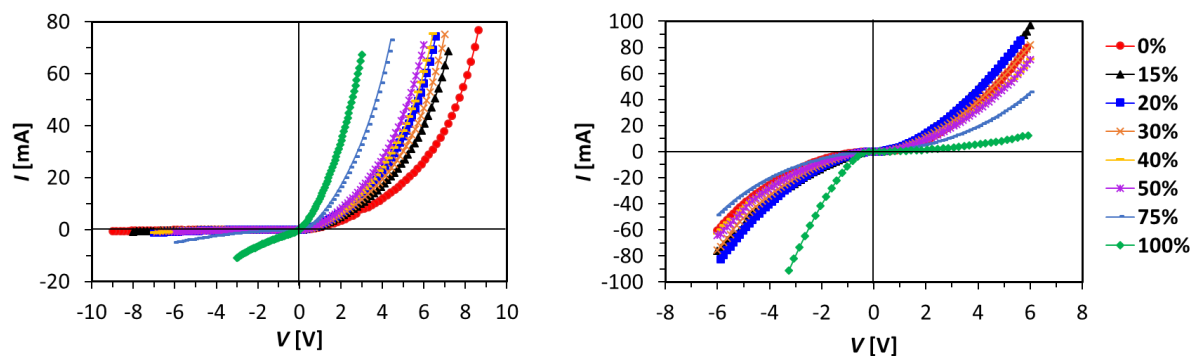


Figure S4. (a) I - V curves of hole only and (b) electron only devices based on different ratios of PC₆₁BM in 4TIC-4F:PC₆₁BM with a PTQ10:acceptors ratio of 1:2.5.

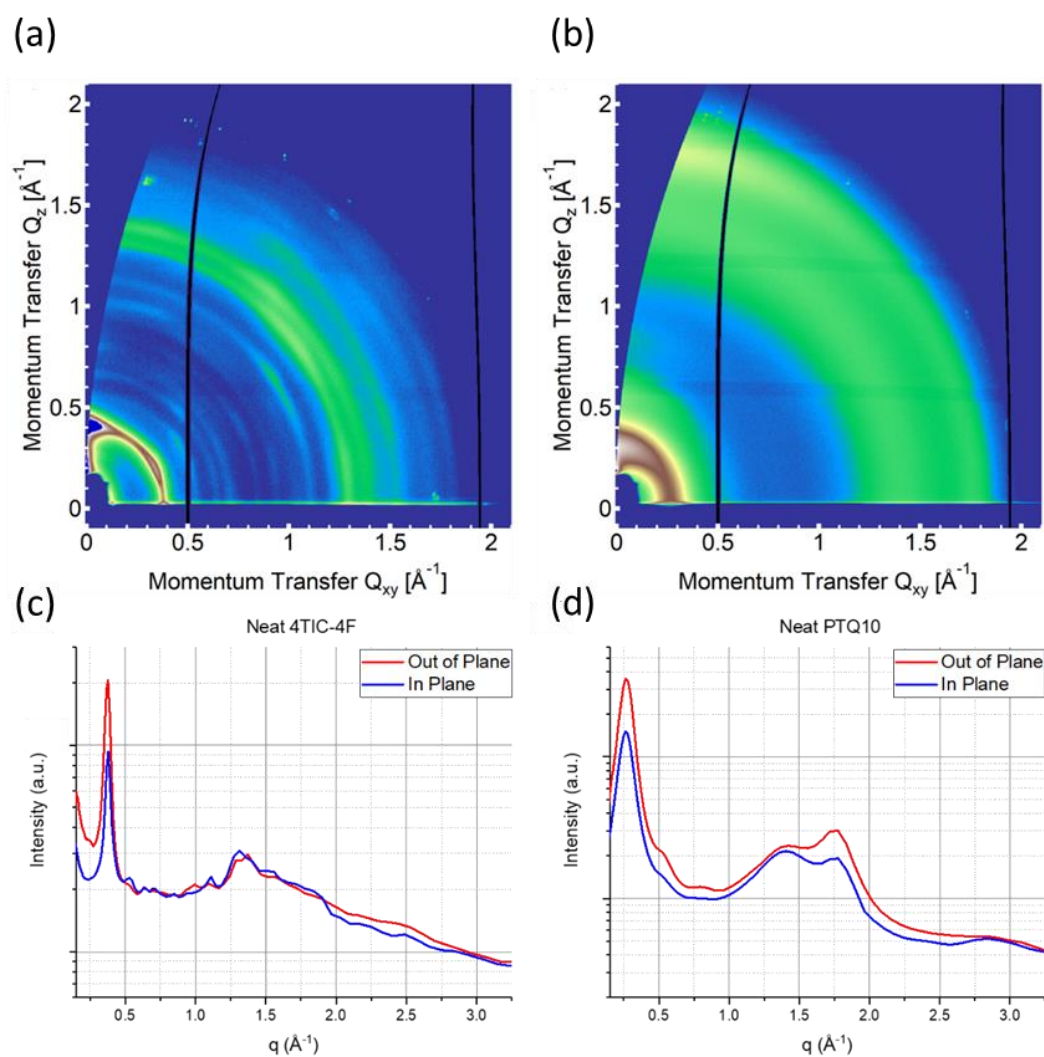


Figure S5. GIWAXS patterns and corresponding IP and OOP line cuts of (a)-(c) neat 4TIC-4F and (b)-(d) neat PTQ10.

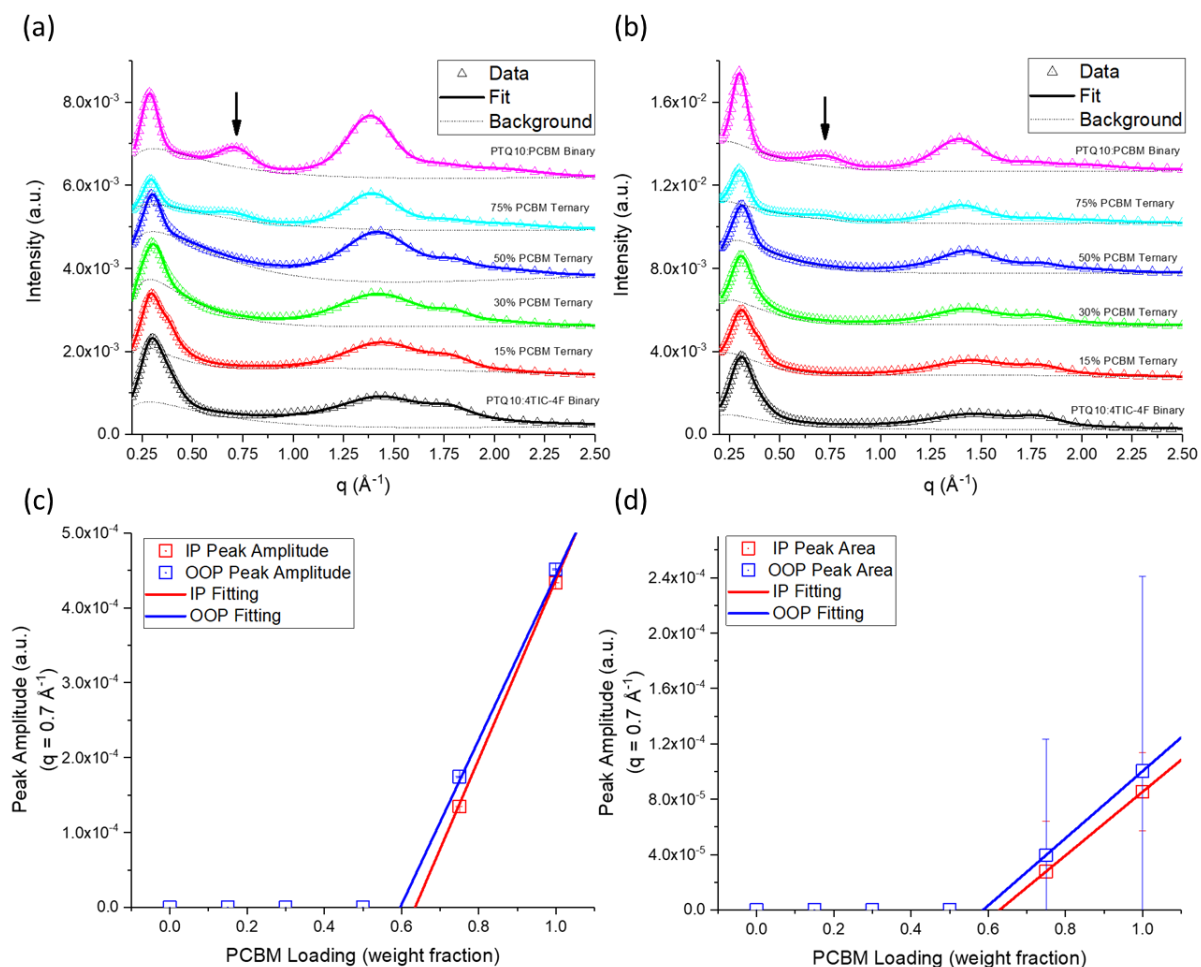


Figure S6. (a) In plane and (b) out of plane 1D line cuts of the GIWAXS data, with multippeak fittings and backgrounds. Arrow indicates the $q = 0.7 \text{ \AA}^{-1}$ PC₆₁BM peak of interest. (c) The fitted amplitude and (d) the fitted area of the PC₆₁BM peak.

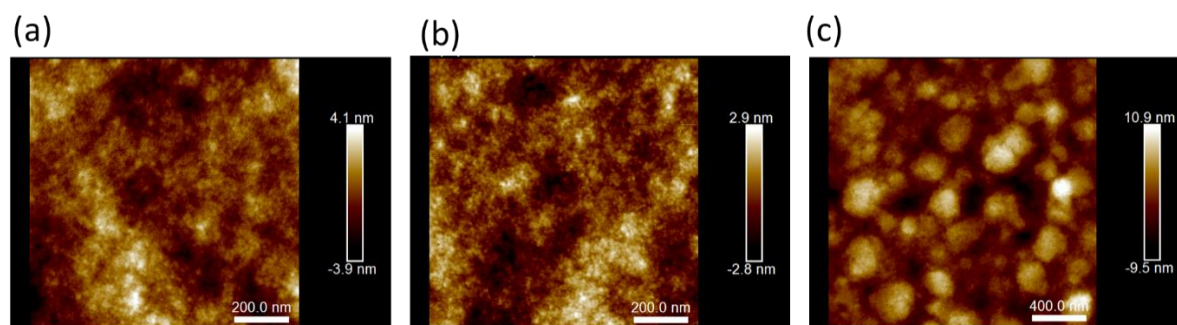


Figure S7. AFM height images of (a) PTQ10:4TIC-4F (b) PTQ10:4TIC-4F:PC₆₁BM (c) PTQ10:PC₆₁BM.

Details of the surface energy and interfacial tension calculations and values

The Wu's model, , takes into account a harmonic mean:

$$\gamma_L \cdot (1 + \cos(\theta)) = 4 \cdot \frac{\gamma_L^d \cdot \gamma_S^d}{\gamma_L^d + \gamma_S^d} + 4 \cdot \frac{\gamma_L^p \cdot \gamma_S^p}{\gamma_L^p + \gamma_S^p}$$

Equation S4. Wu's model equation^[S16]

In this equation, θ is the static contact angle between the solvent and the film, γ_L^d and γ_L^p are the dispersive and polar components of the solvent, γ_S^d and γ_S^p are the dispersive and polar components of the film, γ_L and γ_S are the total surface energy *i.e.* the sum of the dispersive and polar components. The used components for each solvent are the following ones: $\gamma_{\text{Water}}^d = 21.8 \text{ mN.m}^{-1}$; $\gamma_{\text{Water}}^p = 51 \text{ mN.m}^{-1}$; $\gamma_{\text{EG}}^d = 30.9 \text{ mN.m}^{-1}$ and $\gamma_{\text{EG}}^p = 47.7 \text{ mN.m}^{-1}$. The contact angles values, the goniometer pictures and the corresponding surface energy values are summarized in **Table S6** and **Figure S8**.

Table S6. Contact angles with EG and water and calculated surface energies of pristine PTQ10, 4TIC-4F and PC₆₁BM with the Wu's method.

Material	Solvent	Contact angle θ [°] ^{a)}	γ_a [mN.m ⁻¹]	γ_p [mN.m ⁻¹]	γ_o [mN.m ⁻¹]
PTQ10	Water	108.37 ± 0.05	20.7	1.9	22.6
	EG	79.43 ± 0.39			
4TIC-4F	Water	90.95 ± 0.24	17.5	9.8	27.3
	EG	62.99 ± 0.36			
PC ₆₁ BM	Water	84.48 ± 0.60	12.6	15.7	28.2
	EG	64.60 ± 0.71			

a) The standard deviations are based on measurements of three different films using two drops of solvent for each film.

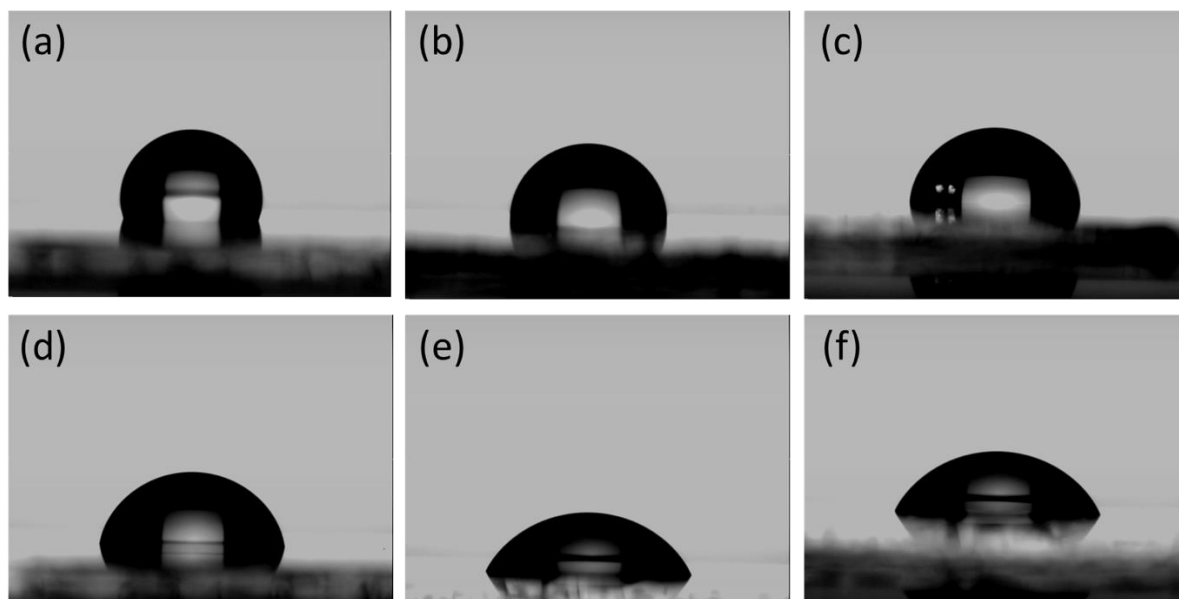


Figure S8. Goniometer pictures of contact angles with water and (a) PTQ10 (b) 4TIC-4F (c) PC₆₁BM films and EG with (d) PTQ10 (e) 4TIC-4F (f) PC₆₁BM films.

The interfacial tension γ_{AB} between two organic semiconductors A and B was calculated using the Equation S5:

$$\gamma_{AB} = \gamma_A + \gamma_B - \frac{4\gamma_A^d\gamma_B^d}{\gamma_A^d + \gamma_B^d} - \frac{4\gamma_A^p\gamma_B^p}{\gamma_A^p + \gamma_B^p}$$

Equation S5. Determination of the interfacial tension between two organic semiconductors.

Table S7. Interfacial energy between each couple of materials.

Material A and B	γ_{AB} [mN.m ⁻¹]
PTQ10 & 4TIC-4F	5.5
PTQ10 & PC ₆₁ BM	12.7
4TIC-4F & PC ₆₁ BM	2.2

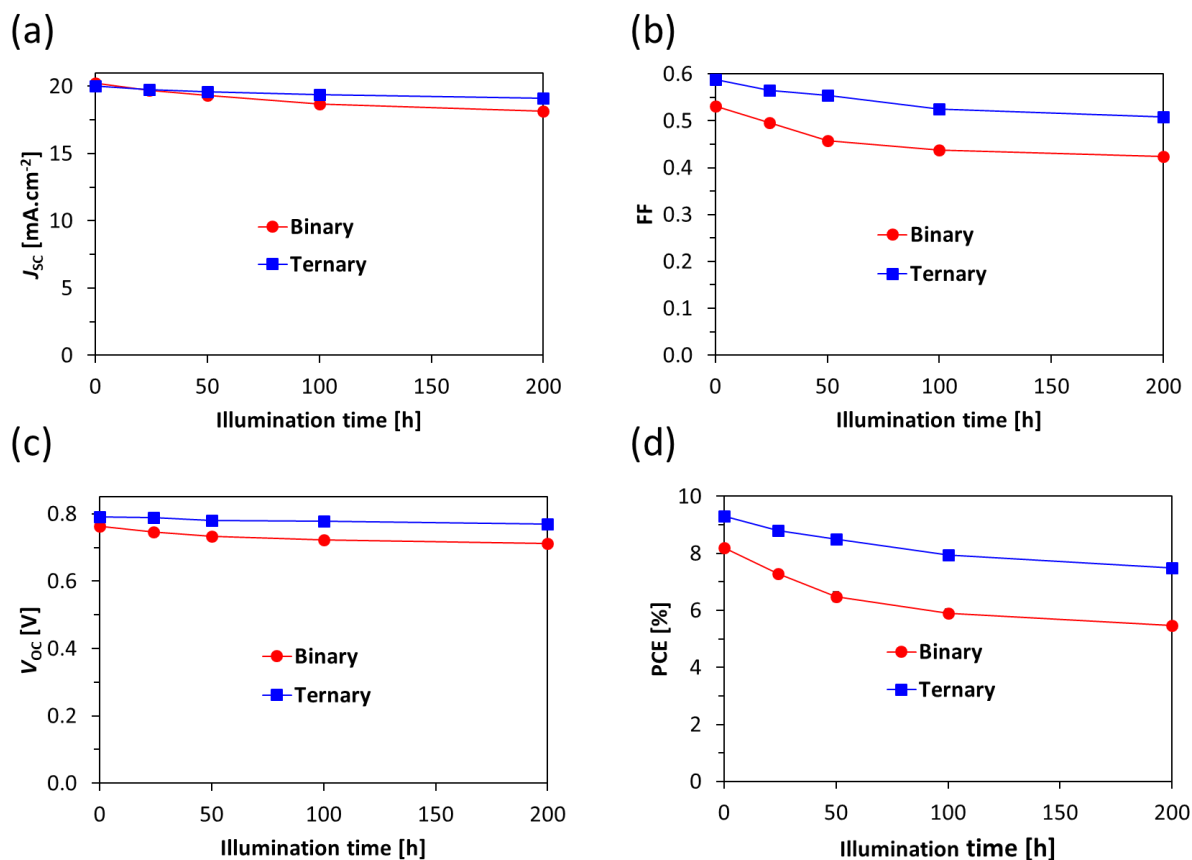


Figure S9. Evolution of the (a) V_{oc} (b) J_{sc} (c) FF and (d) PCE with different 1-SUN illumination times.

References for supporting information

- [S1] A. Hexemer, W. Bras, J. Glossinger, E. Schaible, E. Gann, R. Kirian, A. MacDowell, M. Church, B. Rude, H. Padmore, J. Phys. Conf. Ser. 2010, 247, 012007.
- [S2] R. Po, G. Bianchi, C. Carbonera, A. Pellegrino, *Macromolecules* **2015**, 48, 453.

- [S3] C. L. Chochos, M. Spanos, A. Katsouras, E. Tatsi, S. Drakopoulou, V. G. Gregoriou, A. Avgeropoulos, *Prog. Polym. Sci.* 2019, 91, 51.
- [S4] Z.-P. Yu, Z.-X. Liu, F.-X. Chen, R. Qin, T.-K. Lau, J.-L. Yin, X. Kong, X. Lu, M. Shi, C.-Z. Li, H. Chen, *Nat. Commun.* 2019, 10, 2152.
- [S5] D. Yuan, F. Pan, L. Zhang, H. Jiang, M. Chen, W. Tang, G. Qin, Y. Cao, J. Chen, *Sol. RRL* 2020, 2000062.
- [S6] X. Shi, X. Liao, K. Gao, L. Zuo, J. Chen, J. Zhao, F. Liu, Y. Chen, A. K. Y. Jen, *Adv. Funct. Mater.* 2018, 28, 1802324.
- [S7] H. Yao, Y. Cui, R. Yu, B. Gao, H. Zhang, J. Hou, *Angew. Chemie - Int. Ed.* 2017, 56, 3045.
- [S8] T. Kunz, P. Knochel, *Chem. - A Eur. J.* 2011, 17, 866.
- [S9] X. Shi, L. Zuo, S. B. Jo, K. Gao, F. Lin, F. Liu, A. K. Y. Jen, *Chem. Mater.* 2017, 29, 8369.
- [S10] M. Ueda, N. Imai, S. Yoshida, H. Yasuda, T. Fukuyama, I. Ryu, *European J. Org. Chem.* 2017, 6483.
- [S11] R. Kumar, S. Naqvi, N. Gupta, S. Chand, *RSC Adv.* 2014, 4, 15675.
- [S12] C. Sun, F. Pan, H. Bin, J. Zhang, L. Xue, B. Qiu, Z. Wei, Z.-G. Zhang, Y. Li, *Nat. Commun.* 2018, 9, 743.
- [S13] S. Dai, T. Li, W. Wang, Y. Xiao, T. K. Lau, Z. Li, K. Liu, X. Lu, X. Zhan, *Adv. Mater.* 2018, 30, 1706571.
- [S14] D. Baran, R. S. Ashraf, D. A. Hanifi, M. Abdelsamie, N. Gasparini, J. A. Röhr, S. Holliday, A. Wadsworth, S. Lockett, M. Neophytou, C. J. M. Emmott, J. Nelson, C. J. Brabec, A. Amassian, A. Salleo, T. Kirchartz, J. R. Durrant, I. McCulloch, *Nat. Mater.* 2017, 16, 363.
- [S15] P. P. Khlyabich, A. E. Rudenko, R. A. Street, B. C. Thompson, *ACS Appl. Mater. Interfaces* 2014, 6, 9913.
- [S16] S. Wu, *J. Polym. Sci. Part C Polym. Symp.* 1971, 34, 19.